Acta Materialia 179 (2019) 107–118

Contents lists available at ScienceDirect

Acta Materialia

journal homepage: www.elsevier.com/locate/actamat

Designing solid solution hardening to retain uniform ductility while quadrupling yield strength

Ping-Jiong Yang [a], Qing-Jie Li [b], Wei-Zhong Han [a, *], Ju Li [c], Evan Ma [b, **]

[a] Center for Advancing Materials Performance from the Nanoscale, State Key Laboratory for Mechanical Behavior of Materials, Xi'an Jiaotong University, Xi'an, 710049, China
[b] Department of Materials Science and Engineering, Johns Hopkins University, Baltimore, MD, 21218, USA
[c] Department of Nuclear Science and Engineering and Department of Materials Science and Engineering, Massachusetts Institute of Technology, Cambridge, MA, 02139, USA

ARTICLE INFO

Article history:
Received 19 May 2019
Received in revised form
18 July 2019
Accepted 14 August 2019
Available online 17 August 2019

Keywords:
Oxygen interstitial
Dislocation trapping
Strain hardening
Back stress

ABSTRACT

Single-phase metals can be strengthened via cold work, grain refinement, or solid solution hardening. But the yield strength elevation normally comes at the expense of ductility, i.e., a conspicuous decrease of the uniform elongation in uniaxial tension. This strength-ductility trade-off is often a result of inadequate strain hardening rate that can no longer keep up with the elevated flow stress to prevent plastic instability. Here we alleviate this dilemma by designing oxygen interstitial solution hardening in body-centered-cubic niobium: the strain hardening rate is exceptionally high, such that most of the uniform tensile ductility of Nb can be retained despite of quadrupled yield strength. The oxygen solutes impose random force field on moving dislocation line, promoting the formation of cross-kinks that dynamically accumulate vacancy-oxygen complexes. These obstacles enhance the trapping/multiplication of screw dislocations as well as cross-slip, all promoting strain hardening and strain de-localization. This approach utilizes only a low concentration of interstitial solutes to achieve effective strengthening and strain hardening simultaneously, and is an inexpensive and scalable route amenable to the processing of bulk samples.

1. Introduction

Metals are commonly strengthened via grain size refinement (grain boundary hardening), cold work (dislocation storage), solid solution hardening, and precipitation hardening. These routes normally sacrifice much of the hallmark ductility of metals [1–3], i.e., the large uniform tensile strain (ε_u) before plastic instability sets in. This is because the defects purposely introduced into the metal to elevate the yield strength (σ_y) make it difficult to efficiently store additional defects needed for a high strain hardening rate (Θ) during uniaxial tensile deformation. In fact, Θ usually becomes lower than that in the un-strengthened metal, or is in any case inadequate to keep up with the elevated flow stress (σ) to prevent the plastic instability predicted by the Considère criterion ($\Theta < \sigma$). This leads to an early onset of strain localization, limiting the uniform elongation achievable in uniaxial tension. An example has been shown in Ref. 3: when strengthening gives a four-fold increase in yield strength σ_y, the uniform ductility ε_u often drops by more than a factor of four.

This well-known strength-ductility trade-off [1,2] has been the subject of extensive research in recent years. By engineering the internal grain structure, in particular heterogeneities and gradients such as grains of different sizes, hierarchical twins and stacking faults, a number of success stories have been reported, producing strength–ductility combinations that are superior to those observed for conventional microstructures [3–6]. However, the goal of a much-elevated yield strength together with little reduction in uniform tensile ductility remains difficult to realize [3–10]. In fact, even when multiphase microstructures are used to reach a higher strain hardening rate from second-phase precipitates [11,12] and particles [13–16], or from phase transformations known for TRIP steels [17,18], the uniform ductility achieved is still not as high as that of an un-strengthened metal. Also, if one involves precipitation hardening, to avoid brittle second phases the alloy design

* Corresponding author.
** Corresponding author.
E-mail addresses: wzhanxjtu@mail.xjtu.edu.cn (W.-Z. Han), ema@jhu.edu (E. Ma).

https://doi.org/10.1016/j.actamat.2019.08.024
1359-6454/

and processing tend to be more costly and time-consuming.

Here we illustrate that for single-phase metals, solid solution hardening does not necessarily have to be accompanied by a major sacrifice of uniform ductility, unlike grain size and cold work strengthening. Our idea is to judiciously choose solutes that not only effectively harden the matrix metal, but also markedly increase the strain hardening capability at the same time. For example, interstitial solutes like C, N and O have been well known to be highly effective in solid solution hardening, especially in body-centered-cubic (BCC) metals [19–23]. Meanwhile, these solutes also increase the strain hardening rate by a large margin [19,21,23] (the reasons will be uncovered and discussed later). The oxygen (solute) - niobium (host metal) system appears to be a good example in this regard: there is only a minor degradation of ε_u, when σ_y is raised by as much as a factor of four, as will be demonstrated in this work. To pursue strength-ductility synergy in such single-phase solution alloys, the solute concentration needs to be not only below the equilibrium solubility in the host metal to avoid the precipitation of brittle second phases, but also sufficiently low to prevent damage initiation mechanisms that lead to oxygen embrittlement [21–24].

This “low concentration of oxygen solutes into matrix” route also furnishes other benefits. First, gaseous solutes can be readily added into liquid metals at high temperatures. Alternatively, by controlling the temperature and surface oxygen partial pressure, these interstitial solutes can be charged deep into the bulk solid; interstitials can diffuse millimeters into the bulk, in contrast with the micrometers gradient layer from surface mechanical attrition [7]. Traditionally, surface carburization and nitridation have been widely utilized for improving wear resistance and corrosion resistance [19,25,26], but there the concentration of the alloying elements can be rather high to precipitate out a second phase.

2. Materials and methods

2.1. Oxygen charging

Pure Nb (99.95%) with grain size of ~70 μm was annealed at 1050 °C for 2 h under the vacuum of $\sim 5 \times 10^{-4}$ Pa [21]. Then the dog-bone-shaped tensile bars, with a gauge length of 27 mm and diameter of 4 mm, were fabricated by machining and subsequent mechanical grinding. After cleaning in acetone, the tensile bars were put in the tube furnace to acquire a solute oxygen gradient (SOG), by oxygen charging at 1000 °C for 1 h (SOG-1 Nb) and 3 h (SOG-2 Nb), respectively, as shown in the inset of Fig. 1(a). This was followed by furnace cooling. To suppress the massive formation of surface oxides, the pressure inside the tube was set to 270 Pa using a mechanical pump with continuously flowing of 0.2% O_2/Ar atmosphere. Finally, the bars were mechanically ground to remove surface oxides (1–2 μm in thickness) for mechanical testing.

Nb samples with uniform oxygen distribution (UO Nb) were also prepared, as shown in Fig. 1(b). They were treated with the same processing procedure as SOG-1 and SOG-2 Nb, but then annealed at 10^{-4} Pa for 10 h to obtain UO-1 and UO-2 samples. Therefore, the overall oxygen solute concentration in the UO-1 and UO-2 Nb samples is the same as that in SOG-1 and SOG-2 Nb, respectively. The recrystallization temperature is 1075 °C for pure Nb, such that oxygen charging and subsequent annealing at 1000 °C do not change the grain size of SOG Nb and UO Nb [27]. The carbon, nitrogen, oxygen concentration was measured using a LECO ONH836 Oxygen/Nitrogen/Hydrogen Elemental Analyser and a LECO CS844 Carbon/Sulfur Analyser. The initial niobium contains 74 wppm O (~0.04 at%), <20 wppm N and <20 wppm C.

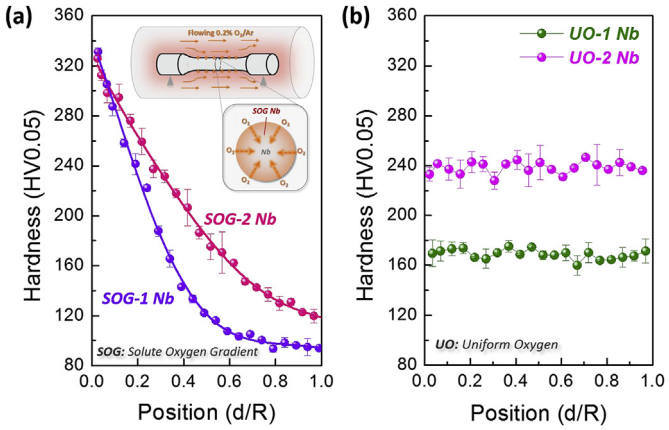

Fig. 1. Effect of solute oxygen gradient (SOG) and uniform oxygen distribution (UO) on the hardness of Nb. (a) Hardness distribution of coarse-grain Nb with two different solute oxygen gradient distributions. The inset is the sketch of the oxygen charging process to form solute gradients. (b) Hardness distribution of coarse-grain Nb with two different uniform oxygen distributions. R is the cross-section diameter and d is the distance from the sample surface to the tested position on the cross section of the sample. Note that the overall oxygen concentration in UO-1 and UO-2 Nb sample is the same as that in SOG-1 and SOG-2 Nb, respectively.

2.2. Mechanical testing

Vickers hardness measurement along the radial direction of the specimens was performed with the maximum applied load of 50 g and a holding time of 10 s. Two or three points were tested for each position to ensure reproducibility. The quasi-static tensile tests were conducted using SANS CMT4104 tensile machine at a strain rate of 10^{-3} s^{-1}. MTS extensometer was used to measure the strain. At least three samples were tested for each case and all the repeated test curves show similar behavior. The loading-unloading-reloading test was performed to measure the back stress. The loading and reloading were performed in a displacement-control mode at an estimated rate of 10^{-3} s^{-1}, while the unloading process was conducted in a load-control mode at the loading rate of 50 N/s [28,29]. As the estimated average strain rate during unloading should be no more than 10^{-4} s^{-1}, the unloading process is of quasi-static deformation mode. In this case, the difference between displacement-control mode and load-controlled mode should not distinctly affect the unloading curve here.

2.3. Microstructure analysis

HITACHI SU6600 SEM was used for fracture surface analysis. A high-resolution TEM (JEOL 2100F) operating at 200 KV was utilized for dislocation characterization at different depth from sample surface. The sample for TEM characterization was cut from the uniformly deformed region of the tensile bar (far away from the neck and its affected zone). Then slices with dimensions of ~1.5 mm × 3 mm and thickness of ~0.5 mm were cut from regions at various depths from sample surface. After being ground to ~60 μm, the slices were further dimpled to ~20 μm using M200 Dimpling Grinder and finally thinned via ion milling.

2.4. Electrochemical test

The sample for electrochemical test was connected to copper wires by tin soldering and molded in a resin, with the surface area of ~10 cm × 10 cm exposed for electrochemical test. The sample was polished to remove surface oxides and contamination. A conventional three-electrode system was used for electrochemical test.

A calomel electrode and a platinum sheet were used as the reference and counter electrodes, respectively. After 10 min immersion in 1 M NaCl to reach a stable open circuit potential, the potentiodynamic polarization (PDP) measurements were performed with a scan rate of 10 mV/min at room temperature. Electrochemical impedance test was performed with a sinusoidal voltage of 5 mV between the frequencies of 0.01 Hz and 10^5 Hz.

2.5. Molecular dynamics simulations

Classical molecular dynamics (MD) simulation has been employed to provide atomistic insights into the observed solid solution hardening. Such simulations are usually limited by its intrinsic timescale, length scale and the accuracy of interatomic potentials. We therefore have paid special attention to setting up and interpreting our simulations. Specifically, the empirical interatomic potential adopted in this work has been developed to describe a wide range of defect properties in the Nb–O system, including generalized stacking fault energy, screw dislocation core structure, Peierls barrier, point defects, and the intricate interactions among various defects. An example application of this interatomic potential can be found in our previous work investigating oxygen embrittlement of Nb [21].

Due to the short timescale or high strain rates in typical MD simulations, our simulations are meant to provide qualitative understanding to help interpret mechanism involved in laboratory samples, rather than directly comparing specific numerical values/parameters to experimental results. For example, experimentally ~0.5 at.% oxygen leads to solid solution hardening while ~1.0 at.% oxygen induces embrittlement [21]; however, simulations with higher strain rates suggest that nano-cavities already take shape at ~0.5 at.% oxygen concentration [21]. Therefore, in this work we use relatively lower oxygen concentration (0.3 at.%), instead of the exact experimental one, to compensate for the high strain rate effects (i.e., to avoid early damage initiation). On the other hand, the yielding/flow stress of BCC metals is highly sensitive to strain rates due to thermally activated motion processes of screw dislocation. Consequently, high strain rates in MD simulations may lead to similarly high stresses in both Nb and Nb–O samples, diminishing the hardening effects of oxygen solutes. As such, if hardening effects can be observed in MD simulations, we expect similar or even stronger hardening effects in our laboratory experiments. We focus on the qualitative interpretation of the hardening effects in terms of the atomistic mechanisms uncovered in our MD simulations.

To evaluate oxygen induced hardening effects in MD simulations, we carried out two sets of MD simulations. The first focuses on the microstructure changes and the resultant flow stress variations, as a long screw dislocation repeatedly moves through the random arrays of oxygen interstitials. The second set of simulations are designed to investigate the respective influence of oxygen interstitials and vacancy-oxygen (V–O) complex on screw dislocation motion. Both sets of simulations share the same crystal orientations, i.e., both screw dislocation line sense and Burgers vector are aligned in [111] direction, while the slip plane normal direction (free surface boundary condition) and dislocation motion direction (periodic boundary condition) are along $[1\bar{2}1]$ and $[\bar{1}01]$, respectively. However, in the first set of simulations, a much longer dislocation line (218 nm) and free surfaces along the line sense direction were used to fully develop the defect microstructure. In contrast, only a shorter segment of screw dislocation (26 nm) with periodic boundary conditions were adopted to investigate the pinning effects of oxygen interstitials and V–O complex. In general, if the dislocation line length is much longer than the mean free path of kinks, then boundary conditions are not expected to impose significant influence on the defect formation and evolution. Simple shear with a strain rate of 10^7 s^{-1} was imposed by assigning atomic velocities to fixed surface atoms. For more simulation details, see Ref. [21].

3. Results and discussion

3.1. Strengthening with little sacrifice of uniform ductility

The inset of Fig. 1(a) is a schematic showing a dog-bone-shaped polycrystalline coarse-grain Nb tensile bar with the diameter of ~4 mm. During heating in the tube furnace, gaseous O_2 can be efficiently catalyzed to form oxygen atoms [30,31] and quickly diffuse from the oxygen-concentrated surface into the bulk interior. As explained in the preceding section, we have prepared two types of samples. The first type has a solute oxygen gradient (shown in Fig. 1(a), hereafter referred to as SOG). The second type has a uniform oxygen concentration (shown in Fig. 1(b), hereafter referred to as UO). The oxygen induced hardening scales monotonously with oxygen concentration [32], such that the hardness depth profile in Fig. 1 can be used to gauge the oxygen concentration and its distribution profile. In Fig. 1(a), two representative gradient (labelled 'SOG-1 Nb' and 'SOG-2 Nb') samples have an oxygen concentration gradually decreasing from the surface (at <1 at% O, below the solubility limit of ~1.4 at.% in Nb [33]) into the inner matrix. Note that the oxygen has penetrated to a distance over 2 mm, two orders of magnitude deeper than that produced via surface treatments such as severe surface mechanical attrition [7]. The average oxygen concentration is ~0.54 at% in SOG-1 Nb and ~0.69 at% in SOG-2 Nb. No obvious increase in carbon or nitrogen content was detected. Samples with uniform solute oxygen distribution (labelled 'UO-1 Nb' and 'UO-2 Nb') are shown in Fig. 1(b) (see details in 2.1). They have the same overall oxygen content as SOG-1 Nb and SOG-2 Nb, respectively, but were homogenized via long-term high vacuum annealing.

The engineering tensile stress-strain curves of SOG Nb are shown in Fig. 2(a) (see Fig. 3 for true stress-strain curves); the yield strength of SOG Nb reached 3.5 times that of the coarse-grain Nb without oxygen charging treatment (hereafter referred to as CG Nb). Note that this latter CG Nb control sample actually contains impurities (including ~74 wppm O, or 0.04 at%). If compared with pure Nb [34], the yield strength after oxygen solution hardening is approximately a factor of 4 higher. This quadrupled yield strength greatly improves the specific strength of Nb, to the level close to Ti (the most commonly used bone implant material, see Section 3.7). Importantly, the quadrupled strength came with only minor reduction of uniform elongation, as marked on the curves in Fig. 2(a). Furthermore, the area under the stress-strain curve becomes much larger. Similar stress-strain curves with similar behavior, i.e., quadrupled yield strength without drastic decrease of uniform strain, can also be seen in UO Nb. As shown in Fig. 2(b), a stress drop is obvious at the beginning of yielding, suggesting solute atmosphere around dislocations after long-term annealing (The difference between SOG Nb and UO Nb will be discussed later).

The well-known Considère criterion indicates that an elevated strain hardening capability should be available, to retain the uniform elongation despite of the much elevated strength. To see this, the strain hardening rate Θ is plotted versus tensile strain in Fig. 3. Clearly, both SOG Nb and UO Nb sustains a much higher strain hardening rate than CG Nb over a wide range of plastic strain. Moreover, increased oxygen content contributes to higher strain hardening capability, as seen in Fig. 3. Apparently, the interstitial solute can simultaneously elevate the yield strength and the strain hardening rate. The high strain hardening rate sustains uniform tensile strain. This is because based on the Considère criterion, necking sets in at the strain where the strain hardening rate equals

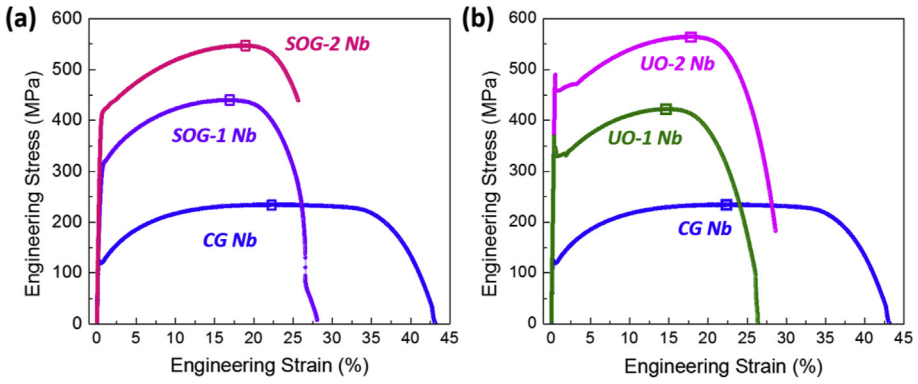

Fig. 2. Effect of solute oxygen gradient (SOG) and uniform oxygen distribution (UO) on the tensile behavior of Nb. (a) Engineering stress-strain curve of coarse-grain Nb (CG Nb) and CG Nb with oxygen gradient (SOG-1 Nb and SOG-2 Nb, respectively). (b) Engineering stress-strain curve of CG Nb with uniform oxygen distribution (UO-1 Nb and UO-2 Nb, respectively). The uniform elongation of each curve is marked by hollow boxes.

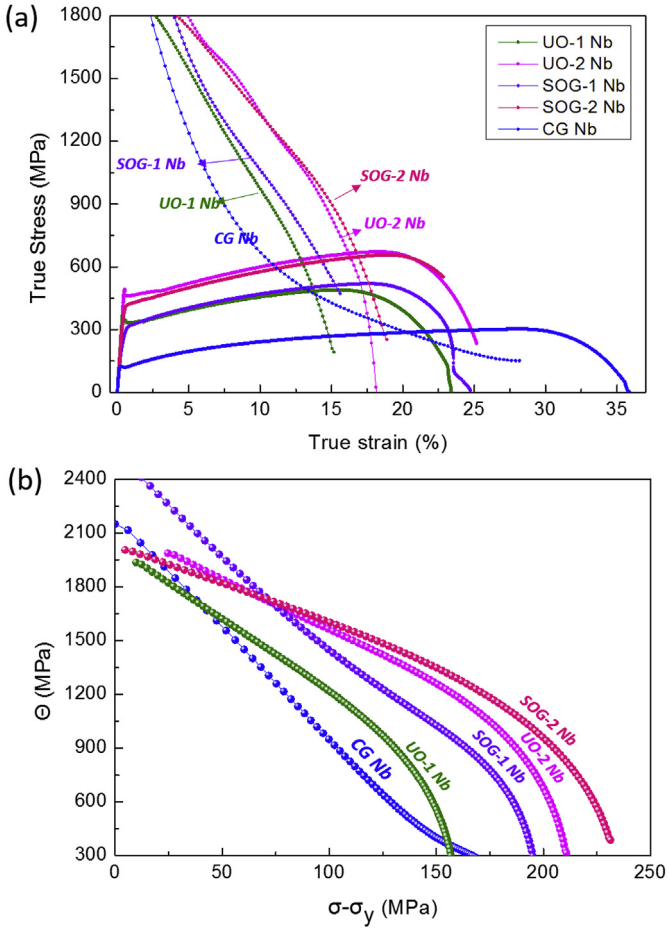

Fig. 3. Comparison of strain hardening curve among CG Nb, SOG-1 Nb, SOG-2 Nb, UO-1 Nb and UO-2 Nb. (a) True stress-strain curve and corresponding strain hardening rate verse true strain curve. (b) Strain hardening rate Θ verse σ-σ_y curve. (Here Θ is the strain hardening rate, σ is the true stress and σ_y is the yielding stress from the true stress-strain curve.)

true stress. This instability is delayed to a strain over 20%, as seen in Fig. 3 for SOG-2 and UO-2.

3.2. Strengthening and strain hardening mechanism

We now explain why a solute concentration of <1 at% O can quadruple the yield strength of Nb, and at the same time work harden the metal so effectively upon straining. It is well known that oxygen in the compressed octahedral interstitial site in the BCC crystal structure causes significant asymmetric lattice distortions. The large distortions, both shear and dilatational, interact strongly with both edge and screw dislocations to give potent hardening. This is akin to the case of C interstitials in the body-centered tetragonal (BCT) martensite in steels: when supersaturated to well beyond the equilibrium solubility of 0.002 wt% (0.0093 at%) in Fe, the interstitial C enhances the martensite strength by a factor of 2–3, compared with ferrite where the C supersaturation is released [35].

For oxygen in Nb, the hardening mechanism is actually more complicated [21]. In particular, as will be demonstrated below using MD simulations, a low concentration of oxygen solutes can lead to several progressive pinning effects on screw dislocations. Let us first show, based on MD simulations, how the microstructure changes as a long screw dislocation moves through the randomly distributed oxygen solutes. Fig. 4 shows both the shear stress profile and typical MD snapshots within a time period of 28 ns. Under the applied constant strain rate, the shear stress varies in an intermittent way, leading to quasi-periodic cycles characterized by a nearly elastic loading followed by a steep stress drop. Although such quasi-periodic variations are inherent to MD simulations (e.g., originated from small sample dimensions and the applied strain rates etc.), the 'elastic' loading feature and higher peak stresses do indicate pinning effects. As an example, without pinning in Fig. 5, pure Nb shows both intermittent loading and lower peak stresses. As can be seen in Fig. 4(b–c), a long screw dislocation moving through the random force field of oxygen interstitials generates profuse point defects and dislocation dipoles/prismatic loops, suggesting additional dragging resistance to screw dislocations. Note that the initial decreasing peak stress form B to D in Fig. 4(a) is mainly due to the reaction between screw dislocation and the dipoles/prismatic loops (Fig. 4(d)), which accelerates the elastic energy release. Similar phenomenon is also observed at other time such as point E in Fig. 4(a) where a dislocation dipole is dragged out and consequently a much-lowered peak stress follows. Nevertheless, the overall trend is that the peak stresses gradually increases with more passages of screw dislocations.

The overall increase of the peak stress, as seen from point D to G in Fig. 4, is similar to the strain hardening effects observed in our experiments; however, due to limited simulation time and absence of other interacting dislocations that would be expected in real plastic deformation, such a gradual increase of peak stress should be interpreted as a partial contribution to the entire strain

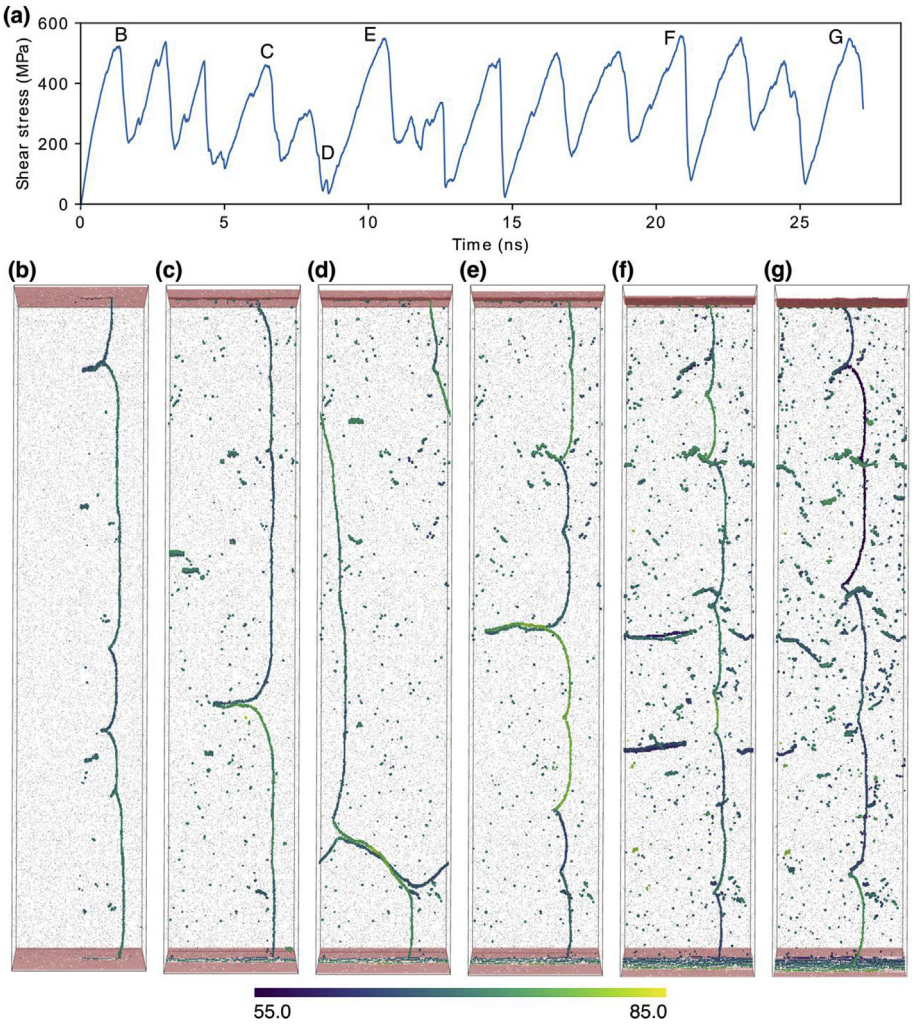

Fig. 4. Microstructure and the corresponding shear stress evolution when a long screw dislocation repeatedly moves through the random array of oxygen interstitials. (a) the shear stress as a function of time. (b–g) dislocation morphologies and various defects configurations that correspond to the points A-G as marked in (a). Dislocation line length is 218 nm. Small gray dots are oxygen interstitials. Atoms on free surfaces are colored in red, while atoms belonging to screw dislocations and various defects are rendered according to their positions along the slip plane normal direction. The color bar (with units of Angstrom) shows the range that the screw dislocation often cross slips. (For interpretation of the references to color in this figure legend, the reader is referred to the Web version of this article.)

hardening. As shown in Fig. 4(e–g), two distinct features of the microstructures can be seen during this stage. First, there is an obvious increase in the number of debris after repeated passages of the screw dislocation. According to our previous work [21], most of these left-over debris are V–O complexes, as both interstitials and vacancies can be easily transported away by passing screw dislocations. Second, there are more pinning sites developed along the screw dislocation line, as can be seen from the cusp configurations in Fig. 4(d–g). This is indicative of a reduction of the mean free path of kinks and also an increasing stress needed to break free from the pinning sites. Specifically, a higher density of pinning sites leads to reduced segment length between two pinning sites, thus higher line tension needs to be overcome as the screw dislocation bows out locally. Such pinned dislocation configurations are consistent with our TEM observations as will be shown in Fig. 6(c). These results suggest that, with increasing strain (i.e., repeated passages of screw dislocations), an increasing number of V–O complexes are created in the Nb–O sample, introducing a growing density of pinning sites that elevate the resistance to dislocation motion and thus harden the material.

To further examine the role played by V–O complexes, we carried out another set of MD simulations on a screw dislocation moving in three different samples. Specifically, pure Nb, Nb+0.3 at% O and Nb+0.3 at%O+0.1 at% V–O were considered. As shown in Fig. 5(a), for the pure Nb sample (green curve), screw dislocation motion results in quasi-periodic fluctuations in shear stress and the peak shear stress is ~340 MPa. However, for the Nb+0.3 at%O sample, the initial shear stress hits a peak at ~410 MPa, suggesting hardening effect. Note that high strain rates in MD simulations often shift the activation regime towards the athermal stress limit [36], i.e., the high stress end on the curve of activation energy vs. stress, thus hardening effects are expected to be relatively smaller, as higher stresses make it hard for obstacles to pin down passing dislocation. Nevertheless, the subsequent peak shear stresses are generally higher than that in pure Nb, occasionally reaching much higher stress levels. The most prominent hardening effect was observed in the sample of Nb+0.3 at% O+0.1 at% V–O. As can be seen in Fig. 5(a), the initial peak stress in this sample reaches ~500 MPa and the subsequent peak stresses are generally higher than that for sample containing only 0.3 at%O, not to mention the pure Nb sample. Furthermore, during prolonged motion, the peak stress can even reach ~600 MPa (t_3 in Fig. 5(a)). Such elevated peak

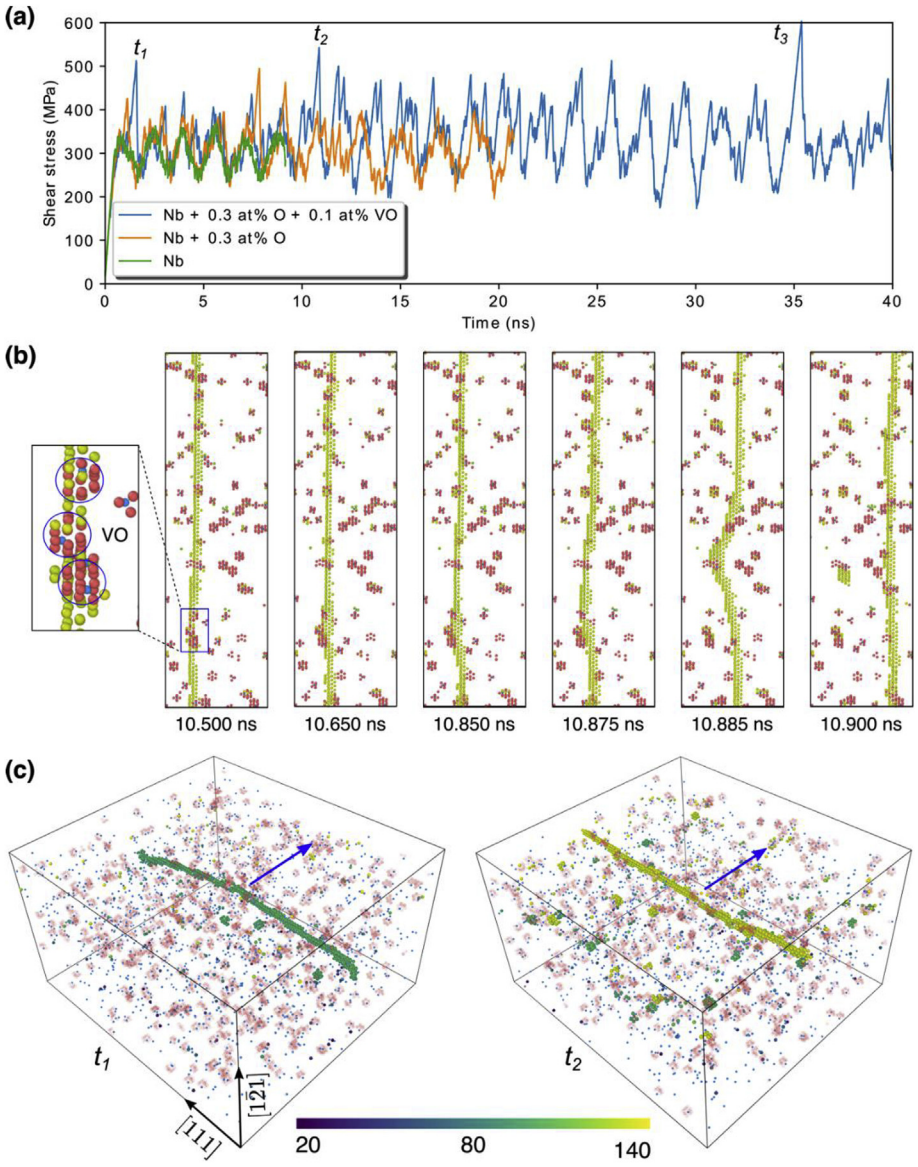

Fig. 5. Pinning effect of V-O complexes on screw dislocation. (a) Shear stress vs. time curves for samples of pure Nb, Nb+0.3 at% O and Nb+0.3 at% O+0.1 at% VO, respectively. (b) Pining effects V-O clusters on screw dislocation. These snapshots were taken within a time period around peak t2. (c) The screw dislocation cross-slips from a middle slip plane to a top slip plane in the simulation box. Oxygen atoms are rendered in blue. The initial V-O complexes are shown as transparent red atom clusters. New defects including screw dislocations and dynamically formed V-O complexes are colored according to their position along the slip plane normal direction. Numbers associated with the color bar are in units of Å. (For interpretation of the references to color in this figure legend, the reader is referred to the Web version of this article.)

shear stresses suggest significant pinning effects on screw dislocation. Fig. 5(b) shows the snapshots around peak t_2 in Fig. 5(a) as an example to demonstrate the pinning effects of V–O complexes. As seen, when the screw dislocation encounters several V–O clusters along the dislocation line, it was trapped for more than 0.375 ns. In contrast, immediately after detrapping, the screw dislocation glides for ~4 nm within a time period of ~0.025 ns. We also noted that, due to significant pinning, the screw dislocation even cross-slips onto parallel slip planes, as shown in Fig. 5(c). Such cross-slip events are desirable as they could further promote dislocation-dislocation interactions and enhance uniform plastic deformation (avoid slip localization). Similar cross-slip enhanced strain-hardening has also been reported in BCC high-entropy alloys with ordered oxygen complexes [15]. On the other hand, the strong pinning effect of V–O complexes can suppress the dynamic recovery of dislocations (a typical softening mechanism in the strain hardening of pure metals). The dynamically production of debris (V–O complexes) are reinforced with increasing strain, prolonging high strain hardening rates and thus uniform elongation.

To recapitulate, we have illustrated that the hardening effect comes from three parts: i) self-pinning due to the readily available cross-kinks formed along the dislocation line, in the random force field of O interstitials; ii) dislocation trapping due to V–O complexes that are dynamically formed with increasing strain; and iii) cross-slips of screw dislocations to get around pinning obstacles. The self-pinning kicks in first as screw dislocations start to move in the random repulsive force field [21], contributing to an elevation of yield stress. After yielding, the motion of screw dislocations creates more and more point defects that further enhance the random force field and self-pinning. Meanwhile, on top of the self-pinning, stabilized V–O complexes further trap screw dislocations in terms of attractive three-body interactions among vacancy,

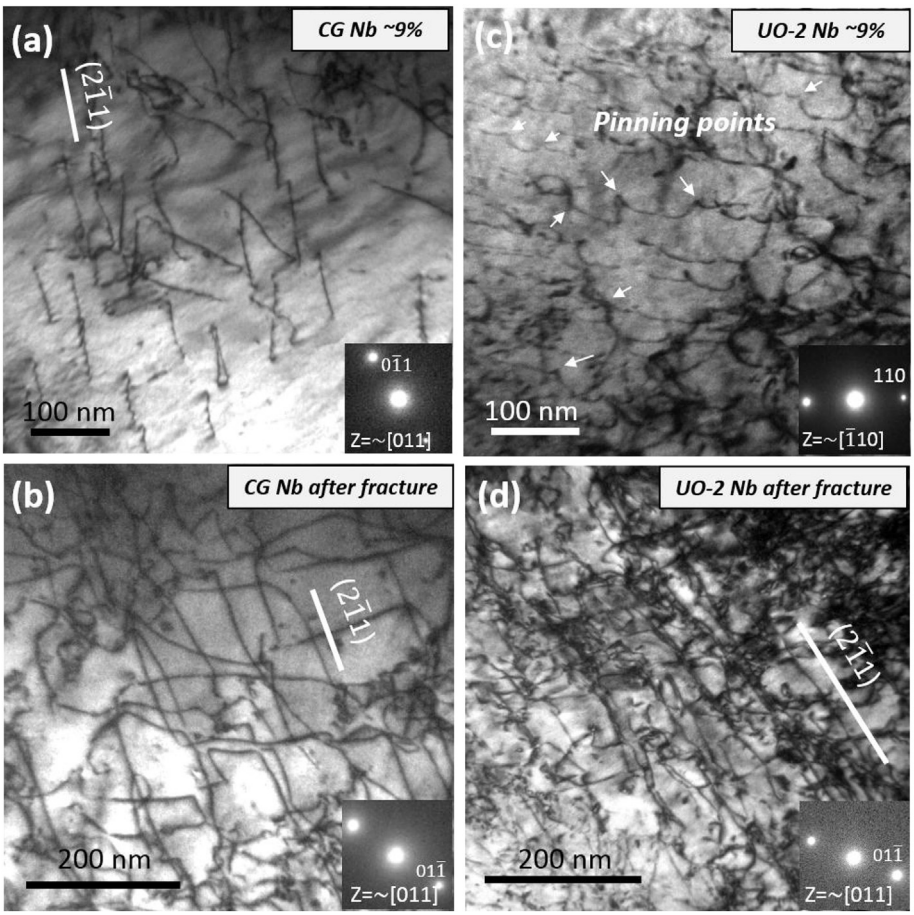

Fig. 6. Dislocation structure of CG Nb and UO-2 Nb during tensile deformation. (a) Dislocation structure of 9% strained CG Nb. (b) Dislocation structure of fractured CG Nb. (c) Dislocation structure of 9% strained UO-2 Nb. (d) The dislocation structure of fractured UO-2 Nb. The TEM samples of fractured CG Nb and UO-2 Nb were sliced at uniform deformation region of the fractured tensile sample. Note that images of (b) and (d) are set as the same magnification. Therefore, direct comparison can be made between these two images.

oxygen and screw dislocation [21]. Due to significant self-pinning and V–O trapping, screw dislocations even cross-slips on to parallel slip planes, further promoting plasticity and dislocation interactions. These three mechanisms together render dislocation motion difficult, causing pronounced dislocation storage and hardening.

3.3. Dislocation structures

To experimentally capture the pinning effect caused by oxygen solutes, dislocation structures were examined under TEM, comparing CG and UO Nb after tensile deformation to various strains, such as 9% plastic strain and after fracture. As shown in Fig. 6(a), typical straight dislocations along {112} planes can be observed for 9%-strained CG Nb. In comparison, for UO-2 Nb the initial long straight dislocations were separated into several curved segments, presumably by strong pinning points, as shown in Fig. 6(c). After further straining, more dislocations have been generated and stored, most of which are aligned along {112} planes (Fig. 6(b) and (d)). Clearly, with the pining effect from oxygen solutes, higher density of dislocations can be stored in Fig. 6(d) compared with Fig. 6(b). These lend credence to the mechanisms discussed in the preceding section: additional dislocation pinning in oxygen-containing samples is indeed at work to accumulate defects to elevate strain hardening.

3.4. The effects of solute gradient

For SOG samples, the deformation is in a plastically non-homogeneous metal, contributing more back stresses that enhance the strain hardening rate. Upon tensile loading the inner part of the SOG Nb sample yields first while the outer oxygen-strengthened part is still in the elastic deformation stage. The migration of dislocations in plastically deforming lower-oxygen part will be hindered by elastically deforming higher oxygen part. The successive yielding in regions of higher and higher oxygen concentration, i.e., a gradual elastic-plastic transition, proceeds along the oxygen gradient, until the whole sample yields macroscopically and stably. This is different from the UO-Nb case, where yielding happens across the entire sample thickness. There the yield point phenomenon suggests solute atmosphere and macroscopically unstable deformation behavior. In comparison, in the SOG-Nb case the yield point phenomenon in local regions would be much less obvious due to the concurrent elastic or steady plastic deformation in the other regions in the sample.

The oxygen and its gradient increases long-range back stresses. This is revealed in loading-unloading-reloading test [8,28,37] shown in Fig. 7. Here for comparison, Nb with uniform solute oxygen distribution was measured (UO-1 Nb), which contains very similar overall oxygen content to SOG-1 Nb. As shown in Fig. 7(a) and (b), wider hysteresis loops are observed for SOG-1 Nb compared with UO-1 Nb and CG Nb. Estimates have been made to

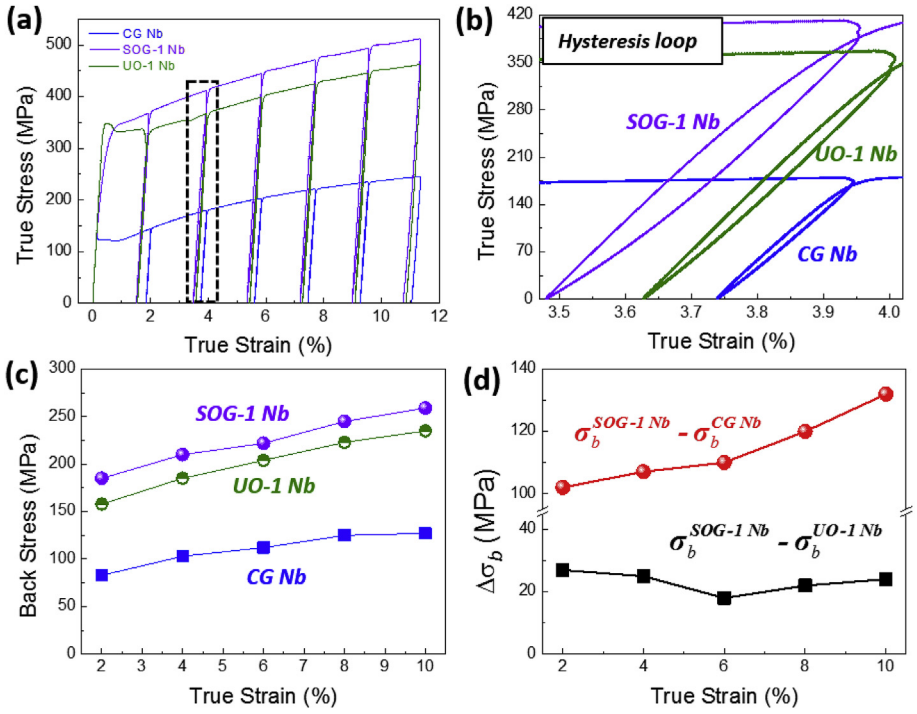

Fig. 7. Back stress of SOG-1 Nb, UO-1 Nb and CG Nb. (a) Loading-Unloading-Reloading curve of CG Nb, UO-1 Nb and SOG-1 Nb. (b) Enlarged view of typical hysteresis loop formed during Loading-Unloading-Reloading test marked by black dashed box in (a). (c) Variation of measured back stress with true strain. (d) SOG induced back stress enhancement compared with CG and UO-1 Nb. The total oxygen concentration in UO-1 Nb is similar to that in SOG-1 Nb.

quantify the back stress and corresponding effective stress, using $\sigma_b = \frac{\sigma_r + \sigma_u}{2}$ and $\sigma_{eff} = \sigma_f - \sigma_b$, where σ_b, σ_{eff}, σ_f, σ_r and σ_u are the back stress, effective stress, flow stress, reloading yield stress and unloading yield stress, respectively. Here the effective stress includes dislocation hardening and Peierls stress [8]. Interestingly, as shown in Fig. 7(c), the back stress of UO-1 Nb is twice that of CG Nb, but less than that of SOG-1 Nb. This suggests that both oxygen interstitials and interstitial gradient contribute to the enhanced back stresses, and hence to the stress hike upon straining (strain hardening). Fig. 7(d) plots the SOG induced back stress strengthening versus tensile strain. As expected, $\Delta\sigma_b^{SOG}$ ($\Delta\sigma_b^{SOG} = \sigma_b^{SOG-1\ Nb} - \sigma_b^{CG\ Nb}$, i.e., enhanced back stress due to oxygen interstitials plus its gradient distribution) monotonously increases with tensile strain. Specifically, as the gradient distribution induced back stress ($\sigma_b^{SOG-1\ Nb} - \sigma_b^{UO-1\ Nb}$) alone nearly remains constant during straining (the black line), the enhancement of back stress is mainly induced by oxygen interstitials; this is consistent with the expected increasing density of pinning dislocations in the presence of oxygen interstitials [21]. The back stress caused by oxygen interstitials here comes from two aspects. First, the large distortion caused by oxygen interstitials stalls dislocations. Second, the dynamically formed V–O complexes during deformation can act as obstacles to trap dislocations. Both of the above effects can lock down dislocations at certain pinning points, forming a strengthened region around the obstacle, surrounded by soft matrix free of obstacles. In this way, plastic strain mismatch arises around the pinning points and leads to the back stress.

In addition, the surface region of the SOG samples should have a compressive residual stress due to the net dilation effect of O interstitial, before any macro deformation. Therefore, if such surface region is fully constrained to lattice-match the core, the triaxial compressive stress can be estimated according to volume expansion and is about 642 MPa on the surface before macroscale deformation. Such a large compressive stress will suppress fatigue/damage micro-crack growth on the surface. Note that the compressive stress developed here is the local stress, only existing in the region with certain oxygen concentration of limited volume. With the decreasing of oxygen concentration from sample surface to the core, the compressive stress shall decrease gradually along the depth. Therefore, the effect of compressive stress as a whole shall not exceed that of the whole yield stress. In reality, there will be some degree of depth-dependent plastic relaxation, generating geometrically necessary dislocations, as discussed earlier for other heterogeneous materials [3,8] (see microstructure images in Fig. 8). Still one would expect a large compressive residual stress on the surface before macro-deformation commences. So even when the surface is subject to damage initiation, the surface damage cracks cannot develop because the local stress is compressive.

To monitor the dislocation microstructure along with SOG induced high back stress discussed above in SOG-1 Nb, TEM characterization has been performed in deformed regions located at various distances from the surface. As shown in Fig. 8, the dislocation configuration changes from curved planar slip near surface to highly tangled multiple slip in the bulk interior. As the inner soft matrix carries more strain during plastic deformation, a high density of tangled dislocations has been produced, as shown in Fig. 8(c). For the part with lower oxygen (Fig. 8(b)), the dislocation starts to show planar feature along the {110} and {112} slip planes. In comparison, the dislocation density decreases near sample surface (Fig. 8(a)). Similar to the pinned dislocations observed in 9%-strained UO-2 Nb (Fig. 6(c)), distinct curved planar slip along {110} planes can be observed in this region, indicating low plastic strain and strong pining effect from oxygen solutes. The planar feature is assumed to originate from the pinning effect caused by V–O complexes [21]. In other words, dislocations can be quickly pinned on certain slip planes by the cluster of oxygen and point defects

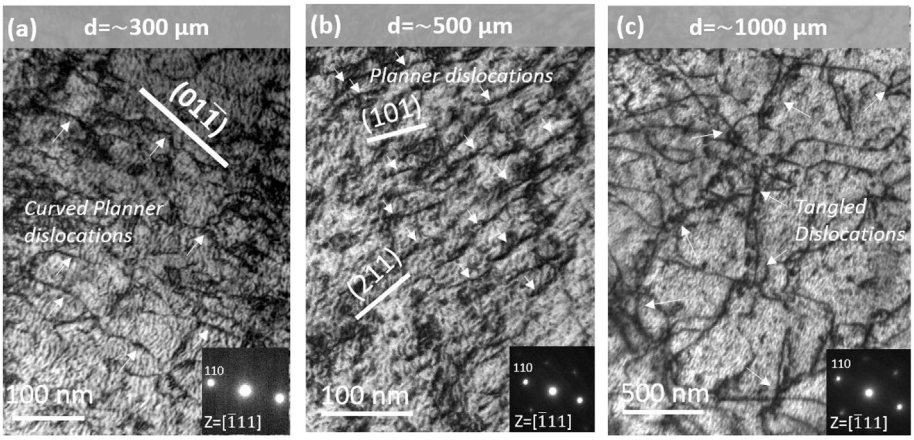

Fig. 8. Dislocation structures of SOG-1 Nb after fracture. (a–c) TEM images of dislocation structures at the position of d ≈ 300 μm, ≈ 500 μm and ≈ 1000 μm from sample surface for SOG-1, respectively. All the samples were taken from uniform deformation region of the tensile bar after fracture.

after nucleation. The inhomogeneous defect distribution shown here is consistent with the idea of plastic strain gradient and GND accumulation that give rise to long-range back stresses (Fig. 7).

3.5. Suppressed embrittlement

Note that our treatment has deliberately maintained the oxygen concentration at a low level, because excessive oxygen solutes are known to cause embrittlement [21,32]. The mechanism can be described as follows [21]: The dynamically formed vacancies, self-interstitials and V–O complexes show different stability during their interaction with passing screw dislocations. Specially, vacancies and self-interstitials will be decomposed while V–O complexes stay put. However, with increasing stress levels and large plastic strains (i.e., extensive passages of screw dislocations), as at the UTS, both the formation and accumulation of stabilized V–O complexes become significant such that nano-cavities will be eventually formed [21]. This would instigate damage during the necking stage, leading to cleavage fracture. The detailed damage initiation process is also shown in our previous work [21]. To observe the eventual damage modes, Fig. 9(a), (b) and (d) show the top view of the fracture surface of CG Nb, SOG-2 Nb and UO-2 Nb, respectively. CG Nb fractures after extensive necking, showing many large-sized dimples with ~60 μm in diameter, as shown in Fig. 9(c). UO-2 Nb also fractures via distinct necking, the resulting dimple size appears to be smaller (<40 μm) than that in CG Nb (Fig. 9(d)). In comparison, SOG-2 Nb exhibits sudden fracture in the late stage of necking, leading to the two distinguishable fracture morphologies in Fig. 9(b), with a boundary marked using dashed white line. While the central part shows typical dimple morphology with sizes comparable to that of CG Nb (Fig. 9(e)), the outer one with more oxygen exhibits fracture features that are more quasi-cleavage like (Fig. 9(f)). Note that in our SOG case, the very thin outer surface layer with <~1 at% oxygen concentration still has the ability to deform to large total strains with strong strain hardening before the damage initiation. The localized slip traces formed on the top surface would not quickly develop into cracks after nucleation (Fig. 10(g)), as the adjacent lower-oxygen region can release localized strain concentration due to its high plastic deformability, in addition to the large compressive residue stress at the top surface. However, with the plastic deformation proceeding, the near-surface region gradually become hardened and lose plastic deformability, eventually nucleating cracks at grain boundaries (Fig. 10(e) and (f)) and facilitating subsequent quasi-cleavage crack

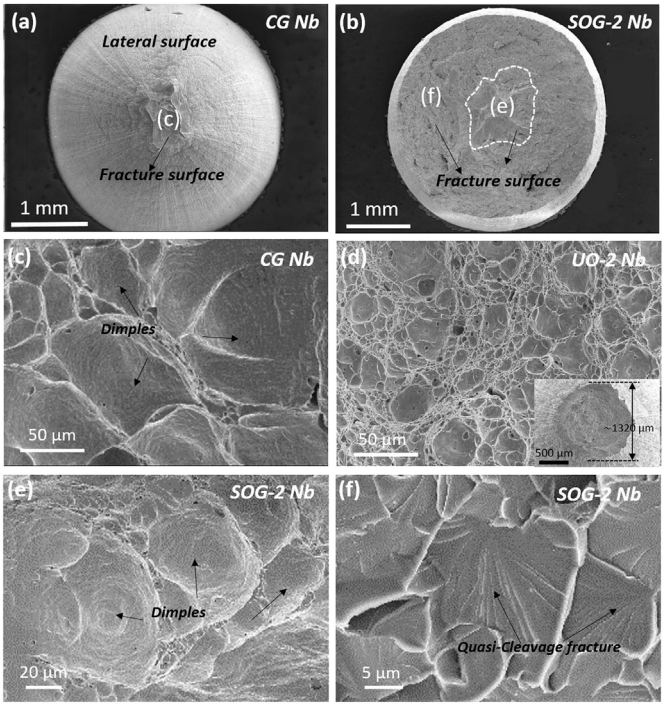

Fig. 9. Fracture surface of CG Nb, UO-2 Nb and SOG-2 Nb. (a) A low magnification SEM image of the fracture surface of CG Nb. (b) A low magnification SEM image of the fracture surface of SOG-2 Nb. (c) An enlarged SEM image of the dimples marked in (a) for CG Nb. (d) An enlarged SEM image of the fracture surface of UO-2 Nb. The inset is the top view of low magnified SEM image of UO-2 Nb. (e,f) Enlarged SEM images of the dimples and quasi-cleavage morphology marked in (b) for SOG-2 Nb.

propagation at the topmost surface (Fig. 10(b)–(d)). This explains why fracture eventually sets in with a quasi-cleavage morphology (Fig. 9(b) and (f)) inside the heavily deformed neck.

3.6. Comparison with previously reported Nb

We now compare our newly developed UO and SOG Nb with other single-phase Nb and its alloys. The yield strength (Fig. 11(a)) and ultimate tensile strength (Fig. 11(b) and 11(c)) are plotted versus uniform strain (uniform percent elongation) or fracture strain (elongation to failure). The shaded area under the dashed curve is the trend previously known for Nb and other metals, i.e.,

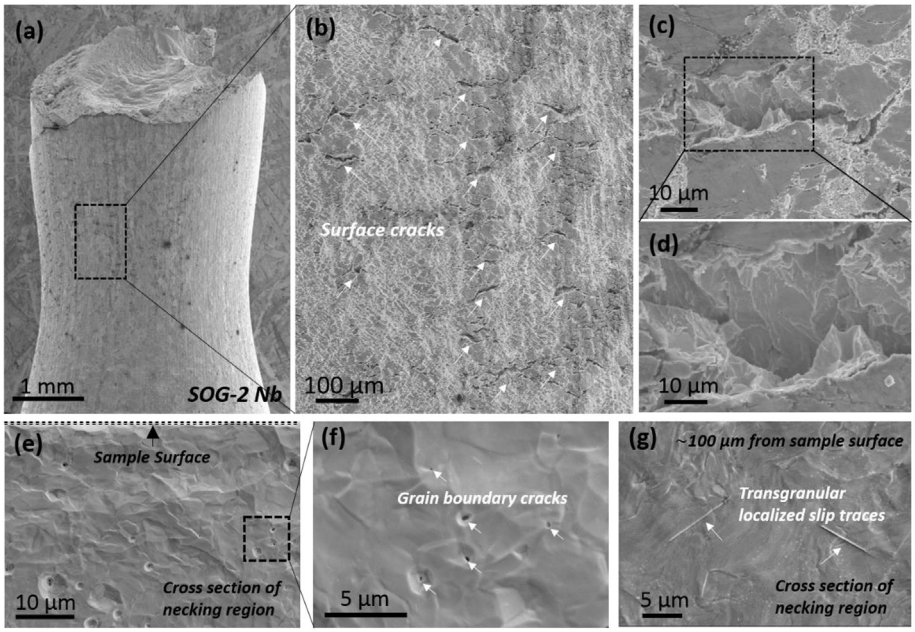

Fig. 10. Lateral surface crack and cross-section microstructure of necking region of SOG-2 Nb after fracture. (a) A low magnified SEM image of the lateral surface at necking region. Brittle fracture happens at the position ~2 mm away from the necking center. (b) A SEM image of high density of cracks on the lateral surface. (c) A magnified SEM of the surface crack. (d) A magnified SEM of quasi-cleavage morphology inside the crack. (e) A low magnified SEM image of near-surface cross-section morphology at necking region. (f) An enlarged SEM image of the grain boundary cracks at the near-surface region. (g) A SEM image of minor transgranular localized slip band at the region ~100 μm away from the sample surface. The cross section of sample at necking region was etched in acid after polishing, hence the grain boundaries and deformation structures can be detected.

the ductility degraded drastically to single digit when the yield strength was raised to a level similar to our UO Nb. The oxygen-solute-hardened Nb clearly stands out [34,39–42], showing a ~20% uniform tensile strain similar to Nb even when the strength is elevated by a factor of four.

In addition to solution hardening without appreciable drop in uniform ductility, another interesting benefit of adding oxygen to Nb is in the area of corrosion resistance. We show next that some solute oxygen concentration at the surface can decrease anodic reaction in corrosive environments. The potentiodynamic tests in 1 M NaCl solution (Fig. 12(a) and Table 1) reveals a more than two-fold reduction of the corrosion current density (I_{corr}) after oxygen charging. Electrochemical impedance spectroscopy in Fig. 12(b) and Table 1 also shows clear improvement of impedance. The increased anti-corrosion resistance is important for Nb alloys as an alternative bioimplant material [43,44]. Beneficial effects are also expected for fatigue resistance: the high yield strength would improve the high-cycle (low cyclic strain) fatigue life, while the low-cycle (high cyclic strain) fatigue resistance may also be improved because of the surface residual compressive stress that make damage initiation difficult [45].

3.7. A potential application

Finally, we mention a specific application that would benefit from the various desirable properties achieved above: the use of Nb as a promising material for making biomedical implants due to its excellent biocompatibility, good ductility, and relatively low Young's modulus [43,44]. The material to compare with is Ti. Normally, Nb has a specific strength (yield strength to density ratio) much lower compared to Ti. In this regard, our solute oxygen strategy to quadruple the strength while preserving uniform ductility would come in handy. The oxygen interstitial diffusivity in Nb is $D_O = 4.55 \times 10^{-7}\exp(-1.1231\text{eV}/k_BT)$ m^2/s [46]. At constant body temperature of 37 °C, the oxygen diffusivity is only 2.56×10^{-25} m^2/s, thus oxygen interstitial would diffuse by only 70 nm in 100 years. This means an engineered oxygen gradient can be preserved in Nb for practical orthopedic applications. On the other hand, at 1000 °C, $D_O = 1.63 \times 10^{-11}$ m^2/s, sufficient to create mm-scale gradient structure within hours of oxygen exposure. By tuning the oxygen gas partial pressure $P_{O2}(t)$ as a function of time t, and temperature $T(t)$, we can "write in" arbitrary oxygen concentration profile $c_O(r)$ inside Nb and be able to utilize its properties at body temperature. Meanwhile, the anti-corrosion and anti-fatigue benefits mentioned in the preceding section further justifies the surface gradient modification. Furthermore, while oxygen solute is used as a demonstration. C and N are expected to work as well via the same mechanism, as discussed in Ref. [21].

4. Summary

Interstitial solutes in a BCC metal, shown above using the oxygen-Nb combination as a model, can simultaneously increase the yield strength, strain hardening rate and ultimate tensile strength, resulting in pronounced hardening (quadrupled yield strength in the Nb case) with little degradation of uniform ductility. This synergistic improvement of mechanical properties, alleviating the strength-ductility trade-off, is not possible for cold work and grain boundary strengthening mechanisms. Our molecular dynamics simulations reveal that the self-pinning due to enhanced cross-kinks formation, strong pinning effect of the dynamically formed V–O complexes and even cross-slips are the dislocation mechanisms underlying the unusually high strain hardening capability, in addition to potent solid solution strengthening. This mechanism, and therefore our strategy is projected to be also effective for other BCC metallic materials (such as Ta and V) that can be effectively strengthened by interstitial solutes. Last but not least, our diffusional introduction of oxygen interstitial solutes is an inexpensive, fast, scalable and programmable process, amenable to bulk samples and practical applications.

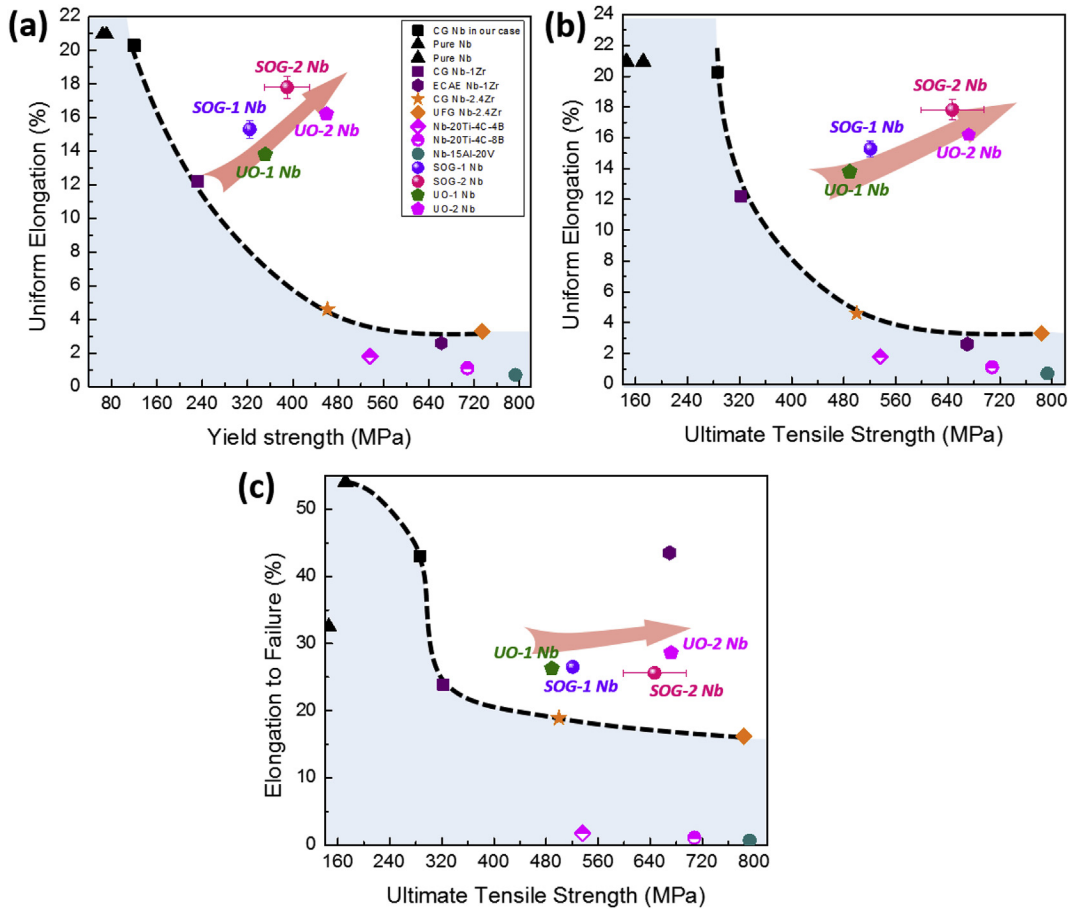

Fig. 11. Tensile elongation versus strength plots for SOG Nb, UO Nb and other Nb alloys. (a) Uniform elongation versus yield strength. (b) Uniform elongation versus ultimate tensile strength. (c) Elongation to failure verse ultimate tensile strength. Data for high purity Nb [34], Nb–Al–V alloys [39], Nb–1Zr alloys [40], Nb-2.4Zr alloys [41], Nb–Ti–C–B alloys [42], and CG Nb are included. The CG Nb used in this study as reference contains a minute amount of impurities including ~74 wppm O (0.04 at%). *The purple point in (c) is a Nb–1Zr alloy with very limited uniform elongation but unexplained high total elongation reported in Ref.* [40]. (For interpretation of the references to color in this figure legend, the reader is referred to the Web version of this article.)

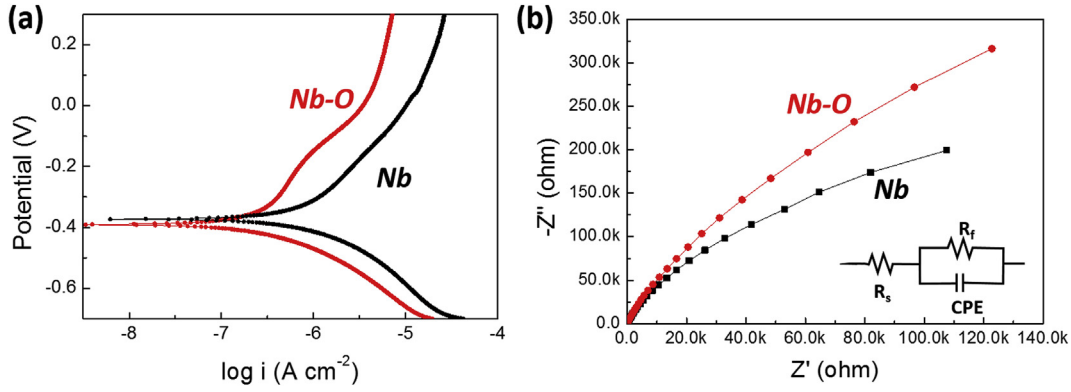

Fig. 12. Corrosion behavior of Nb with solute oxygen (Nb–O) in 1 M NaCl solution. (a) Potentiodynamic polarization (PDP) curve for CG Nb and Nb–O. (b) Nyquist plots from electrochemical impedance spectroscopy (EIS) on CG Nb and Nb–O. The inset is the equivalent circuits for fitting the EIS data during corrosion in our case.

Table 1
Fitting results of Potentiodynamic polarization (PDP) and electrochemical impedance spectroscopy (EIS) plots in Fig. 12.

Sample	PDP test		EIS test			
	E_{corr}/mV	I_{corr}/μA cm^{-2}	R_s/Ω	R_f/MΩ	Y_f/Ω^{-1}cm^{-2}S^{-n}	n_f
CG Nb	−0.366	14.507	6.58	0.649	4.6581E-05	0.9
SOG Nb	−0.391	4.033	11.3	1.55	3.3108E-05	0.89

Acknowledgements

W.Z.H. would like to thank the National Natural Science Foundation of China (Grant Nos. 51922082, 51971170 and 51942104), the National Key Research and Development Program of China (2017YFB0702301) and the 111 Project of China (Grant Number BP2018008). Q.J.L. and E.M. acknowledges the support at JHU by US NSF-DMR-1804320. P.J.Y. would like to thank Bo Yang and Liuyang Sun for their help in electrochemical test and analysis.

References

[1] K. Lu, Making strong nanomaterials ductile with gradients, Science 345 (2014) 1455–1456.
[2] R.O. Ritchie, The conflicts between strength and toughness, Nat. Mater. 10 (2011) 817–822.
[3] E. Ma, T. Zhu, Towards strength–ductility synergy through the design of heterogeneous nanostructures in metals, Mater. Today 20 (2017) 323–331.
[4] Z. Cheng, H. Zhou, Q. Lu, H. Gao, L. Lu, Extra strengthening and work hardening in gradient nanotwinned metals, Science 362 (2018) 6414.
[5] Y. Wei, Y. Li, L. Zhu, L. Yao, X. Lei, G. Wang, Y. Wu, Z. Mi, J. Liu, H. Wang, H. Gao, Evading the strength–ductility trade-off dilemma in steel through gradient hierarchical nanotwins, Nat. Commun. 5 (2014) 3580.
[6] J.W. Zhang, I.J. Beyerlein, W.Z. Han, Hierarchical 3D nanolayered duplex-phase Zr with high strength, strain hardening and ductility, Phys. Rev. Lett. 122 (2019) 255501.
[7] T.H. Fang, W.L. Li, N.R. Tao, K. Lu, Revealing extraordinary intrinsic tensile plasticity in gradient nano-grained copper, Science 331 (2011) 1587–1590.
[8] X. Wu, M. Yang, F. Yuan, G. Wu, Y. Wei, X. Huang, Y. Zhu, Heterogeneous lamella structure unites ultrafine-grain strength with coarse-grain ductility, Proc. Natl. Acad. Sci. U. S. A 112 (2015) 14501–14505.
[9] C.W. Shao, P. Zhang, Y.K. Zhu, Z.J. Zhang, Y.Z. Tian, Z.F. Zhang, Simultaneous improvement of strength and plasticity: additional work-hardening from gradient microstructure, Acta Mater. 145 (2018) 413–415.
[10] Y. Lin, J. Pan J, H.F. Zhou, H.J. Gao, Y. Li, Mechanical properties and optimal grain size distribution profile of gradient grained nickel, Acta Mater. 153 (2018) 279–289.
[11] Y.H. Zhao, X.Z. Liao, S. Cheng, E. Ma, Y.T. Zhu, Simultaneously increasing the ductility and strength of nanostructured alloys, Adv. Mater. 18 (2010) 2280–2283.
[12] S. Cheng, Y.H. Zhao, Y.T. Zhu, E. Ma, Optimizing the strength and ductility of fine structured 2024 Al alloy by nano-precipitation, Acta Mater. 55 (2007) 5822–5832.
[13] G. Liu, G.J. Zhang, F. Jiang, X.D. Ding, Y.J. Sun, J. Sun, E. Ma, Nanostructured high-strength molybdenum alloys with unprecedented tensile ductility, Nat. Mater. 12 (2013) 344–350.
[14] G. Wu, K.C. Chan, L. Zhu, L. Sun, J. Lu, Dual-phase nanostructuring as a route to high-strength magnesium alloys, Nature 545 (2017) 80–83.
[15] Z. Lei, X. Liu, Y. Wu, H. Wang, S. Jiang, S. Wang, X. Hui, Y. Wu, B. Gault, P. Kontis, D. Raabe, L. Gu, Q. Zhang, H. Chen, H. Wang, J. Liu, K. An, Q. Zeng, T.G. Nieh, Z. Lu, Enhanced strength and ductility in a high-entropy alloy via ordered oxygen complexes, Nature 563 (2018) 546–550.
[16] T. Yang, Y.L. Zhao, Y. Tong, Z.B. Jiao, J. Wei, J.X. Cai, X.D. Han, D. Chen, A. Hu, J.J. Kai, K. Lu, Y. Liu, C.T. Liu, Multicomponent intermetallic nanoparticles and superb mechanical behaviors of complex alloys, Science 362 (2018) 933–937.
[17] Z. Li, K.G. Pradeep, Y. Deng, D. Raabe, C.C. Tasan, Metastable high-entropy dual-phase alloys overcome the strength-ductility trade-off, Nature 534 (2016) 227–230.
[18] B.B. He, B. Hu, H.W. Yen, G.J. Cheng, Z.K. Wang, H.W. Luo, M.X. Huang, High dislocation density-induced large ductility in deformed and partitioned steels, Science 357 (2017) 1029.
[19] G.M. Michal, F. Ernst, H. Kahn, Y. Cao, F. Oba, N. Agarwal, A.H. Heuer, Carbon supersaturation due to paraequilibrium carburization: stainless steels with greatly improved mechanical properties, Acta Mater. 54 (2006) 1597–1606.
[20] Q. Yu, L. Qi, T. Tsuru, R. Traylor, D. Rugg, M.J. Jr, M. Asta, D.C. Chrzan, A.M. Minor, Origin of dramatic oxygen solute strengthening effect in titanium, Science 347 (2015) 635–639.
[21] P.J. Yang, Q.J. Li, T. Tsuru, S. Ogata, J.W. Zhang, H.W. Sheng, Z.W. Shan, G. Sha, W.Z. Han, J. Li, E. Ma, Mechanism of hardening and damage initiation in oxygen embrittlement of body-centred-cubic niobium, Acta Mater. 168 (2019) 331–342.
[22] M.G. Jo, P.P. Madakashira, J.Y. Suh, H.N. Han, Effect of oxygen and nitrogen on microstructure and mechanical properties of vanadium, Mater. Sci. Eng., A 675 (2016) 92–98.
[23] R. Roumina, J.D. Embury, O. Bouaziz, H.S. Zurob, Mechanical behavior of a compositionally graded 300M steel, Mater. Sci. Eng., A 578 (2013) 140–149.
[24] H. Shiraishi, K. Furuya, R. Watanabe, Change in solute oxygen level and loss of ductility of niobium during oxidation in imperfect vacuum conditions, J. Less Common. Met. 63 (1979) 147–158.
[25] Y. Sun, X. Li, T. Bell, Low temperature plasma carburising of austenitic stainless steels for improved wear and corrosion resistance, Surf. Eng. 15 (2013) 49–54.
[26] T. Bell, Source Book on Nitriding, American Society for Metals, Metals Park, OH, 1977.
[27] M. Sankar, R.G. Baligidad, A.A. Gokhale, Effect of oxygen on microstructure and mechanical properties of niobium, Mater. Sci. Eng., A 569 (2013) 132–136.
[28] M. Yang, Y. Pan, F. Yuan, Y. Zhu, X. Wu, Back stress strengthening and strain hardening in gradient structure, Mater. Res. Lett. 4 (2016) 145–151.
[29] H. Wang, Z. You, L. Lu, Kinematic and isotropic strain hardening in copper with highly aligned nanoscale twins, Mater. Res. Lett. 6 (2018) 333–338.
[30] N. Birks, G.H. Meier, F.S. Pettit, Introduction to the High-Temperature Oxidation of Metals 2013, Cambridge Univ Pr, 2006.
[31] S. Mathieu, S. Knittel, P. Berthod, S. Mathieu, M. Vilasi, On the oxidation mechanism of niobium-base in situ composites, Corros. Sci. 60 (2012) 181–192.
[32] J.R. Donoso, R.E. Reed-Hill, Slow strain-rate embrittlement of niobium by Oxygen, Metall. Trans. A 7 (1976) 961–965.
[33] R.P. Elliott, Columbium-Oxygen system, Trans. Am. Soc. Met. 52 (1960) 990–1014.
[34] G. Wu, N. Dhanaraj, L. Cooley, D. Hicks, E. Hahn, D. Burk, W. Muranyi, M. Foley, H. Edwards, H. Harms, M. Champion, D. Baars, C. Compton, Tensile tests of niobium materials for SRF cavities, Am. Inst. Phys. 1218 (2010) 857–862.
[35] C.J. Scheuer, R.P. Cardoso, R. Pereira, M. Mafra, S.F. Brunatto, Low temperature plasma carburizing of martensitic stainless steel, Mater. Sci. Eng. A 539 (2012) 369–372.
[36] Q.J. Li, B. Xu, S. Hara, J. Li, E. Ma, Sample-size-dependent surface dislocation nucleation in nanoscale crystals, Acta Mater. 145 (2018) 19–29.
[37] X. Feaugas, On the origin of the tensile flow stress in the stainless steel AISI 316L at 300 K: back stress and effective stress, Acta Mater. 47 (1999) 3617–3632.
[39] H. Jiao, F. Barradas, T. Rong, I.P. Jones, M. Aindow, Observation of tension/compression asymmetry in an Nb–Al–V alloy, Mater. Sci. Eng. A 387 (2004) 476–480.
[40] T. Niendorf, D. Canadinc, H.J. Maier, I. Karaman, G.G. Yapici, Microstructure–mechanical property relationships in ultrafine-grained NbZr, Acta Mater. 55 (2007) 6596–6605.
[41] G. Purcek, O. Saray, F. Rubitschek, T. Niendorf, H.J. Maier, I. Karaman, Effect of internal oxidation on wear behavior of ultrafine-grained Nb–Zr, Acta Mater. 59 (2011) 7683–7769.
[42] X. Zhang, X. He, C. Fan, Y. Li, G. Song, Y. Sun, J. Huang, Microstructural and mechanical characterization of multiphase Nb-based composites from Nb–Ti–C–B system, Int. J. Refract. Metals Hard Mater. 41 (2013) 185–190.
[43] F. Rubitschek, T. Niendorf, I. Karaman, H.J. Maier, Corrosion fatigue behavior of a biocompatible ultrafine-grained niobium alloy in simulated body fluid, J. Mech. Behav. Biomed. Mater. 5 (2012) 181–192.
[44] H. Matsuno, A. Yokoyama, F. Watari, M. Uo, T. Kawasaki, Biocompatibility and osteogenesis of refractory metal implants, titanium, hafnium, niobium, tantalum and rhenium, Biomaterials 22 (2001) 1253–1262.
[45] M. Koyama, Z. Zhang, M.M. Wang, D. Ponge, D. Raabe, K. Tsuzaki, H. Noguchi, C.C. Tasan, Bone-like crack resistance in hierarchical metastable nanolaminate steels, Science 355 (2017) 1055–1057.
[46] R.A. Perkins, R.A.P. Jr, Oxygen diffusion in niobium and Nb-Zr alloys, Acta Metall. 25 (1977) 1221–1230.